Unravelling stacking order in epitaxial bilayer MX_2 using 4D-STEM with unsupervised learning

Reference:
Mehta Ankit Nalin, Gauquelin Nicolas, Nord Magnus, Orekhov Andrey, Bender Hugo, Cerbu Dorin, Verbeeck Johan, Vandervorst Wilfried.- Unravelling stacking order in epitaxial bilayer MX_2 using 4D-STEM with unsupervised learning
Nanotechnology - ISSN 0957-4484 - 31:44(2020), 445702
Full text (Publisher's DOI): https://doi.org/10.1088/1361-6528/ABA5B6
To cite this reference: https://hdl.handle.net/10067/1711190151162165141

Unravelling stacking order in epitaxial bilayer MX2 using 4D-STEM with unsupervised learning

IOP Publishing Nanotechnology
Journal **XX** (XXXX) XXXXXX https://doi.org/XXXX/XXXX

Unravelling stacking order in epitaxial bilayer MX_2 using 4D-STEM with unsupervised learning

Ankit Nalin Mehta,[1,2] Nicolas Gauquelin,[3,4] Magnus Nord,[3,4] Andrey Orekhov,[3,4] Hugo Bender,[1] Dorin Cerbu,[1] Johan Verbeeck,[3,4] Wilfried Vandervorst. [1,2]

[1] imec, Kapeldreef 75, 3001, Leuven, Belgium
[2] KULeuven, Celestijnenlaan 200D, 3001, Leuven, Belgium
[3] EMAT, Groenenborgerlaan 171, 2020, Antwerp, Belgium
[4] NANOlab Center of Excellence, University of Antwerp, Antwerp, Belgium

E-mail: Ankit.NalinMehta@imec.be

Received xxxxxx
Accepted for publication xxxxxx
Published xxxxxx

Abstract

Following an extensive investigation of various monolayer transition metal dichalcogenides (MX_2), research interest has expanded to include multilayer systems. In bilayer MX_2, the stacking order strongly impacts the local band structure as it dictates the local confinement and symmetry. Determination of stacking order in multilayer MX_2 domains usually relies on prior knowledge of in-plane orientations of constituent layers. This is only feasible in case of growth resulting in well-defined triangular domains and not useful in-case of closed layers with hexagonal or irregularly shaped islands. Stacking order can be discerned in the reciprocal space by measuring changes in diffraction peak intensities. Advances in detector technology allow fast acquisition of high-quality four-dimensional datasets which can later be processed to extract useful information such as thickness, orientation, twist and strain. Here, we use 4D scanning transmission electron microscopy (4D-STEM) combined with multislice diffraction simulations to unravel stacking order in epitaxially grown bilayer MoS_2. Machine learning based data segmentation is employed to obtain useful statistics on grain orientation of monolayer and stacking in bilayer MoS_2.

Keywords: Stacking order, bilayer MoS_2, 4D-STEM, DF-TEM

1. Introduction

Molybdenum disulfide (MoS_2) is a prototypical two-dimensional transition metal dichalcogenide with great prospects for applications in nanoelectronics due to its unique optical and electronic properties.[1] It is an n-type semiconductor with a bandgap that ranges between 1.2 – 1.9 eV depending on the layer thickness. [2–4] The band structure of MoS_2 is also sensitive to the stacking order between adjacent layers in bilayer MoS_2 due to interlayer coupling[5], which varies as a function of in-plane twist between the layers[6]. Previous studies investigating spectral differences in bi- or multilayer MoS_2 of various stacking orders rely on material with large and well-defined triangular grains, wherein the orientation of the triangles is used to deduce the stacking order.[7,8] This way to deduce stacking is not useful in case of growth that results in a closed monolayer covered with irregularly shaped nuclei or hexagonal islands. More recent studies have demonstrated electron diffraction-based methods to identify thickness and stacking order in multilayer MX_2.[9,10] These methods utilize the presence of intensity differences among diffraction peaks that vary with the stacking order and can be uniquely identified with the help of diffraction simulations.

Advances in detector technology during recent years has enabled experiments in which a diffraction pattern is acquired quickly and with high sensitivity at every probe position while scanning with a converged electron beam in a Transmission Electron Microscope (STEM). This essentially results in a four-dimensional dataset consisting of 2 navigation dimensions (scan array) and 2 signal dimensions (2D diffraction pattern). This technique is widely known as 4D-STEM[11–16] , although it has been referred to in literature with various other names such as position resolved diffraction

(PRD)[17,18], nanobeam electron diffraction (NBED) [19–21], pixelated STEM[15,22] or scanning electron nanodiffraction [23–25]. While this technique is commonly used for orientation mapping, strain mapping and ptychography, here, we use virtual DF imaging from a 4D dataset to map orientation and stacking order in the CVD deposited epitaxial bilayer MoS_2. A semi-automated method to derive statistical distribution of the stacking order in the layers is developed.

2. Methods

2.1 MoS_2 growth

MoS_2 is deposited on 2" c-plane sapphire using metal organic chemical vapor deposition (MOCVD) similar to the method reported by Chiappe et al..[26] Molybdenum hexacarbonyl ($Mo(CO)_6$) is used as the Mo precursor and dihydrogen sulfide (H_2S) is the S precursor while N_2 is the inert carrier gas. The sapphire substrate is subjected to ex-situ annealing at 1175°C in O_2 ambient for 60 min. Subsequently, the growth is carried out in an MOCVD reactor connected to an ASM Polygon8200 platform. The substrate is heated under N_2/H_2 environment until a growth temperature of 1000°C is reached and allowed to stabilize. H_2S is then introduced into the chamber followed by $Mo(CO)_6$ with a precursor ratio ($H_2S/Mo(CO)_6$) of ~1.2 x 10^4 while the total pressure is maintained at 20 Torr. A post-deposition annealing at 1000°C and 90 Torr in N_2/H_2S ambient is applied on the resulting material. This results in a sample with 1 ML fully closed, partial coverage of 2^{nd} layer islands and minor amounts of 3^{rd} layer islands.

2.2 Specimen preparation and TEM analysis

The TEM specimen is prepared by transferring the material via ultrasonic delamination in warm water using poly(methyl methacrylate) (PMMA) support layer as per the procedure previously reported elsewhere[27]. Bright field (BF) and dark field (DF) TEM analysis is carried out in a TFS Titan G^2 60-300 in Imec operated at 120 kV. Atomic resolution annular dark-field STEM (ADF-STEM) images are acquired with a convergence angle of 23 mrad and STEM detector ranging from 25 to 153 mrad. The 4DSTEM measurements are done in a probe corrected Titan X-Ant-Em at 120kV in EMAT, University of Antwerp (Belgium) which is equipped with a Quantum Detectors Merlin (Medipix) direct electron detection camera. Experiments were carried out in microprobe STEM mode with a convergence angle of 1.5mrad.

2.3 Electron diffraction simulation

Electron diffraction simulations to calculate diffraction peak intensities are carried out using the multislice QSTEM simulation package.[28] The key simulation parameters chosen are close to the experimental conditions with acceleration voltage of 120kV and convergence angle of 1.5 mrad.

2.4 Cluster analysis for image segmentation

Cluster analysis is one of the most common unsupervised learning methods often used to find hidden patterns and groups in exploratory data. A python-based machine learning package called sklearn [29] is applied on the data. Among the several clustering algorithms available in sklearn, the most effective model to fit our data is found to be Variational Bayesian Gaussian Mixture (VBGM). VBGM is a variant of the Gaussian mixture model. This probabilistic model assumes that all the data is generated from a mixture of a finite number of Gaussian distributions with unknown parameters. Variational inference is used for the estimation and is an extension of expectation maximization with added regularization based on information from prior distributions.

The model used is a parametric mixture model estimates the pixel intensity values (x) from a set of correlated images (see Table 2) to be distributed according to a finite number of Gaussian mixture densities. The distribution takes the general form:

$$f(x) = \sum_{i=1}^{k} w_i N(x; \mu_i, \sigma_i)$$

Where k is the number of the Gaussian components, w_i is the weight if each Gaussian component such that:

$$\sum_{i}^{k} w_i = 1, and\ \forall i: w_i \geq 0$$

With $N(x; \mu_i, \sigma_i)$ being the probability density function of the normal distribution. The weights, means and standard deviations for each of the components are defining the gaussian 'blobs' and are iteratively fit to match the experimental data using an expectation maximization algorithm resulting in assigning each pixel intensity to a cluster (component) that isolates a separate layer in the image. This image segmentation can be improved and fully automated by adapting a supervised learning model such as support vector machine (SVM), convolutional neural networks (CNN), random forest (RF), etc., which require labelled datasets as input. This is a topic of great interest for further development but is beyond the scope of this paper.

3. Results

3.1 Mapping stacking order using dark-field TEM

The lack of in-plane inversion symmetry and the mass difference between the Mo and S sublattices in monolayer MoS_2 causes an intensity asymmetry between the {10 -10} diffraction spots separating them into two families (Ka and

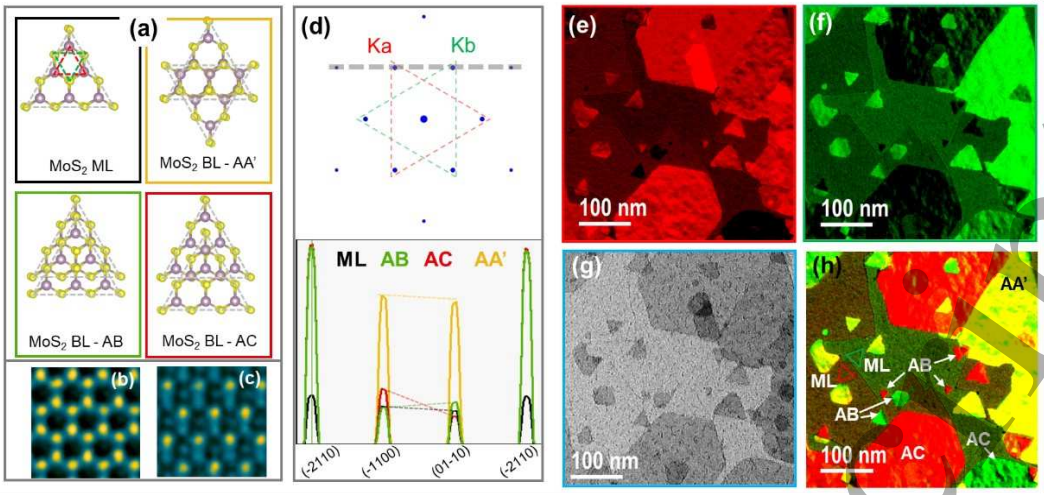

Figure 1: (a) Crystal structures of monolayer MoS_2 and bilayer MoS_2 stacked with AA', AB and AC order. Atomic resolution ADF-STEM images of bilayer MoS_2 in (b) AA' (2H) stacking and (c) AB or AC (3R) stacking. The horizontal direction is zig-zag while the vertical direction is arm-chair. (d) Schematic diffraction pattern where the Ka and Kb spots are highlighted with red and green triangles respectively. Line profiles from simulated CBED patterns (dashed grey line) corresponding to structures shown in (a). (e,f) DF-TEM images of MoS2 grown on sapphire from adjacent {10-10} Bragg spots. (g) Corresponding BF-TEM image from the same area, the brighter and darker regions are monolayer and bilayer respectively. (h) Artificially colored composite image where the colors corresponding to 60° twins in monolayer are dark red and green, and to stacking order in bilayer are bright yellow (AA'), bright green and bright red (either AB or AC). AB or AC can be differentiated based on the color of the underlying monolayer and several regions are labelled for clarity.

Kb) as indicated with the green and the red triangles in the schematic diffraction pattern (Figure 1 (b)). Bilayer Mo S_2 can be stacked in 5 theoretical orders among which two, AA' (2H) and AB/AC (3R) are found to be stable while the remaining are either meta-stable (AB') or unstable (AA, A'B) based on first principle calculations.[5,30] In the following discussion, only the stable stacking orders (AA', AB, AC) are considered since the remaining stacking orders are not observed experimentally using high resolution STEM imaging.

***Table 1:** List of common MX_2 materials with their respective Δ Z values*

Material	Δ Z
WS_2	42
MoS_2	10
WSe_2	6
$MoSe_2$	-26

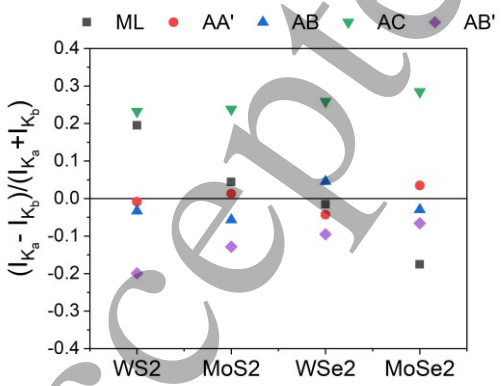

Figure 2: Material and stacking dependence of polarity from simulated CBED patterns

The crystal models of MoS_2 monolayer and bilayer stacked in AA', AB and AC order are shown in Figure 1(a) along with atomic resolution ADF-STEM images of the stable bilayer stacking orders provided in Figure 1(b,c). Both AB and AC are equivalent in symmetry and commonly referred to as 3R phase which lacks inversion symmetry. The difference between AB and AC lies in the atomic order with respect to the electron beam direction where, by convention, the shared atomic columns between the two layers contain Mo on top of S_2 for AC, whereas S_2 on top of Mo for AB stacking. Profiles acquired from simulated CBED patterns from the different structures are shown in Figure 1(d). While asymmetry between K_a and K_b peaks is present for both AB and AC, AC stacking shows a larger asymmetry compared to AB. Moreover, for AB stacking, K_b is larger than K_a which is contrary to the trend for ML and AC ($I_{Ka} > I_{Kb}$). In bilayer stacked AA', the asymmetry almost vanishes due to restoration of in-plane inversion symmetry. Consequently, different bilayer stacking configurations can be differentiated using dark-field TEM images acquired from adjacent {10-10} spots, Figure 1 (e,f). Overlaying these images with artificial colors enhances the contrast variation such that stacking order of a grain can be discerned from its color (Figure 1 (g)). Grains stacked in AA' order have equally bright intensity in both red and green DF-TEM images, thus appearing bright

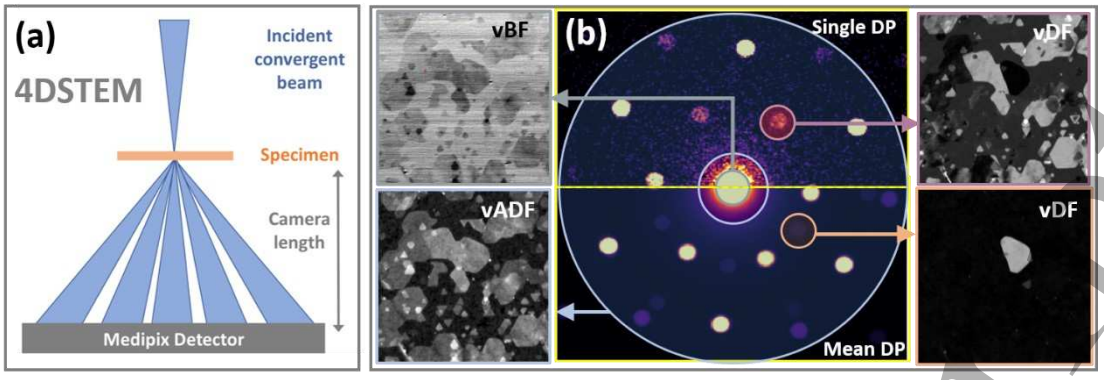

Figure 3: (a) Schematics of 4D-STEM technique. (b) Diffraction pattern from a single pixel (top half) and mean of all pixels (bottom half) along with various virtual aperture positions indicated with coloured circles with the corresponding reconstructed images on each corner.

yellow. Grains stacked as AB (or AC) appear either red or green. Knowledge of the bottom layer's orientation serves as a reference to help distinguish between AB and AC stacking based on orientation of the monolayer. For instance, if the color of the bottom monolayer is red, the brighter red islands are AC stacked whereas bright green are AB. In case of similarly stacked grains, but rotated by 60°, the assigned colors are obviously flipped. This technique has been previously applied to study the nucleation behaviour in a homoepitaxial system which consists of MBE grown WSe_2 on an exfoliated WSe_2 flake.[31]

Figure 2 compares the polarity $[(I_{Ka} - I_{Kb})/(I_{Ka} + I_{Kb})]$ of different 2H-MX_2 in a monolayer and bilayer with different stackings using CBED simulations. The simulated materials are arranged in decreasing order of ΔZ ($\Delta Z = Z(M)-2\times Z(X)$) where a positive correlation with polarity is clearly observed in the monolayer case. This general trend is in good agreement with that reported by Deb et al.[32] However, the polarity for ML – WSe_2 is negative despite a positive ΔZ which differs with Deb's observations. This is thought to be due to minor differences in calculation with their simulations. In AA' stacked bilayer, the polarity is close to 0 in all cases. Intriguingly, in a bilayer stacked in AC or the metastable AB' stacking, the correlation is negative wherein the polarity increases with decreasing ΔZ. AB stacking, on the other hand, does not show any notable trends with respect to ΔZ and oscillates such that W based MX_2 has a higher polarity compared to Mo based MX_2. Nevertheless, the asymmetry is larger for AC than AB in all cases. Therefore, we can assign stacking to colors based on these simulations.

3.2 Mapping stacking order using 4D-STEM

The 4D-STEM measurements on MoS_2 are conducted at EMAT, University of Antwerp, using a direct electron camera (Quantum Detectors Merlin – Medipix) mounted on a probe-corrected Titan cubed microscope. The resulting 4D dataset contains a 2D diffraction pattern at every pixel of the 2D scanning TEM image with little noise as seen in the upper half of the diffraction pattern (Figure 3(b)). The lower half is the mean of all diffraction patterns in the 512 x 512-pixel array. In this lower half of fig. 3b, a small contribution from the 30° rotated grains is evidenced by the faint spots in between the intense spots of the majority orientation. Presence of 30° oriented areas is due to local variation in surface reconstruction of the sapphire substrate used for the initial growth of the MoS_2 monolayer. Using pyXem[33], a python-based library built to process 4D-STEM datasets, different parts of the diffraction patterns can be integrated using virtual apertures to obtain virtual BF, DF or annular DF (ADF) images as shown on each corner of Figure 3(b).

Six virtual DF (vDF) images are extracted from each of the {10-10} diffraction spots defining 2 subsets of 3 spots represented by 2 triangles rotated by 60° with respect to each other. Similar to figure 1(g), composite images are formed by overlaying different pairs of these DF images in Figure 4 either using opposite spots (also known as Friedel's pairs), in top panels a, or using adjacent spots, in bottom panels b. The colors of bilayer islands differ significantly among these sets of images depending on which pair of spots is chosen. This is most evident in composite images from adjacent spots where a green island in one image appears red in the other, resulting in an ambiguous interpretation of stacking (AB vs AC). Difference in contrast between these DF images is in fact related to the presence of a minor sample tilt with respect to the e-beam during the experiment. The effect of such tilt is illustrated in figure 4 (c,d) by comparing simulated CBED patterns of AC stacked structure without any tilt to a similar stacking tilted by 1° in the arm-chair direction. The relationship between intensities of the 3 Ka spots $I(Ka_1)=I(Ka_2)=I(Ka_3)$ and the 3 Kb spots $I(Kb_1)=I(Kb_2)=I(Kb_3)$ in untilted AC simulation no longer holds true in presence of a small tilt where the relative intensities of spots change considerably $I(Ka_1)\neq I(Ka_2)\neq I(Ka_3)$ and similarly $I(Kb_1)\neq I(Kb_2)\neq I(Kb_3)$. Note that despite variation in contrast, the color of the monolayer regions

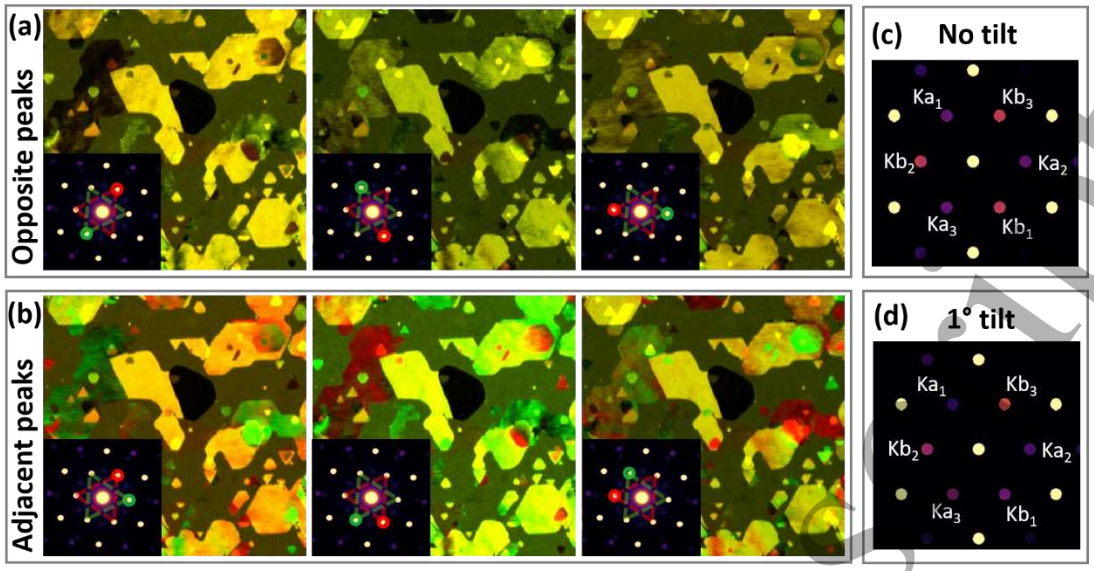

Figure 4: Composite vDF images formed using (a) opposite and (b) adjacent peaks, respectively. Insets show the positions of the virtual aperture. Simulated CBED patterns for AC stacked MoS_2 with (c) no tilt and (d) 1° tilt along the armchair axis.

remains unchanged and its orientation determination is unaffected by the presence of tilt.

A simple way to minimize the influence of small sample tilts is by summing the 3 vDF images from the red aperture positions and the 3 from the green, ultimately resulting in 2 images which are overlaid with the respective artificial colors $Ka=Ka_1+Ka_2+Ka_3$ and $Kb=Kb_1+Kb_2+Kb_3$. To verify the efficacy of this operation in reducing minor tilt effects, CBED simulations are done for ML and other possible stacking orders in bilayer (AA', AB, AC, AB') with tilt up to 3° along both zig-zag and armchair axes. The results are shown in Figure 5 wherein the polarity $[(I_{Ka}-I_{Kb})/(I_{Ka}+I_{Kb})]$ is plotted as a function of stacking order using a single pair of adjacent or opposite peaks in comparison to the summed peaks case. When considering a single pair of peaks, we find that while the influence of tilt is minimal for ML and bilayer with AA' stacking, the polarity for other stacking orders diverges from

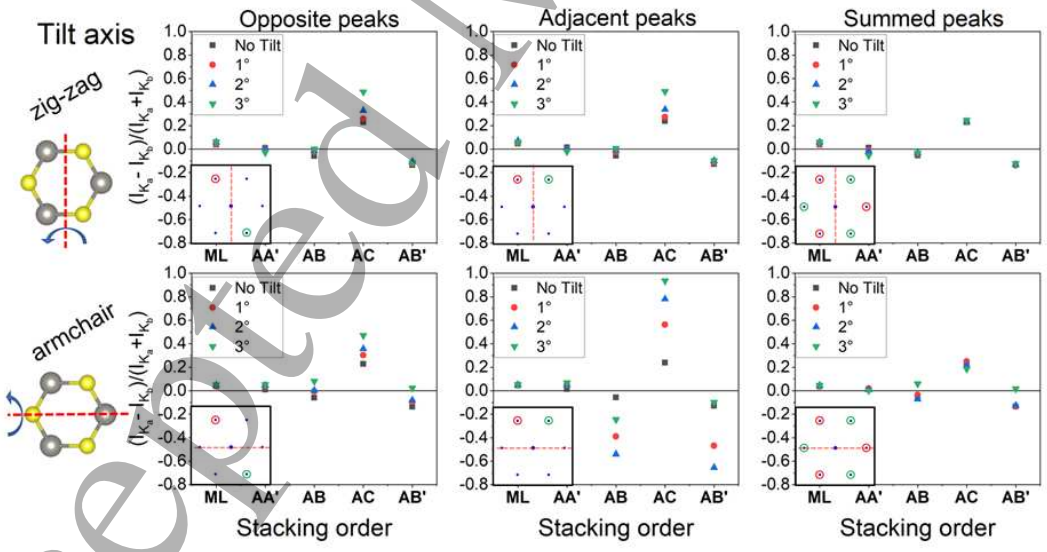

Figure 5: Influence of tilt on polarity $[(I_{Ka}-I_{Kb})/(I_{Ka}+I_{Kb})]$as a function of stacking order using a single pair of opposite peaks (left), pair of adjacent peaks (center) and sum of 3 Ka and 3 Kb peaks (right). The tilt axis is along the zig-zag direction for the top row and armchair for the bottom row as depicted in the schematic on the far left. The inset on bottom-left of each plot depicts the selected Ka (red) and Kb (green) peaks and the dotted red line represents the tilt axis. CBED simulations used for these data are done at 120 kV with a convergence angle of 1.5 mrad to replicate experimental conditions.

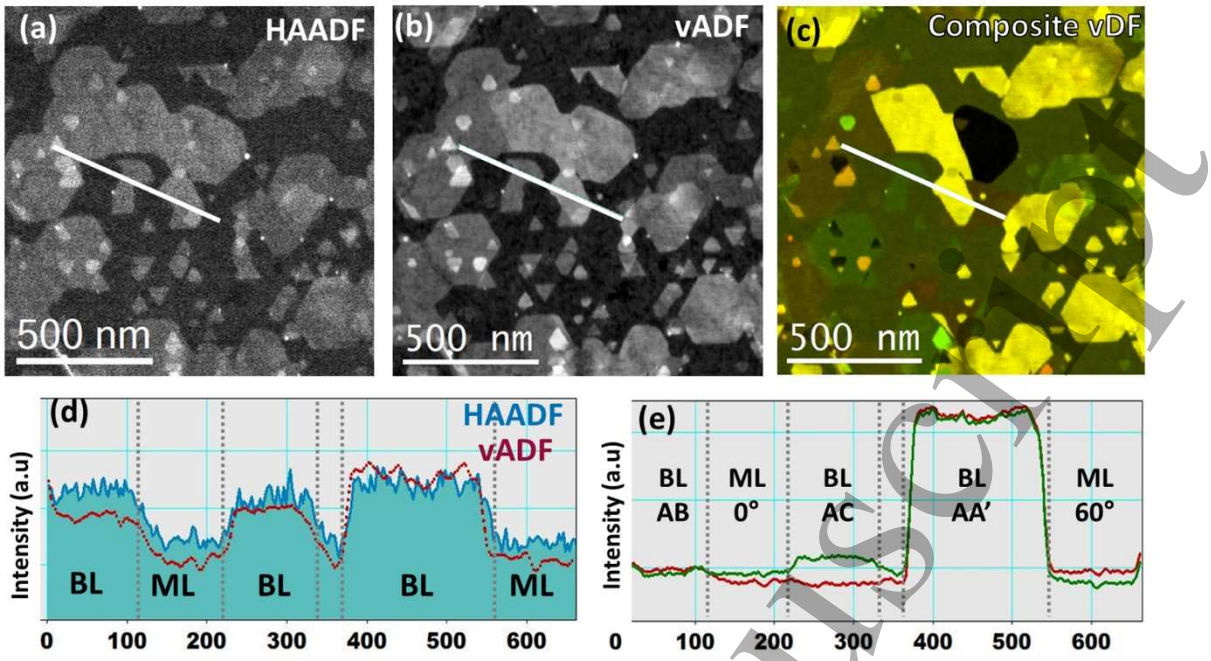

Figure 6: (a) HAADF STEM image acquired in the same region prior to 4D-STEM acquisition. (b) Virtual ADF image and (c) composite virtual DF image reconstructed from the 512 x 512 4D dataset by summing 3 Ka and 3 Kb. (d) Line profiles comparing HAADF and ADF intensities. Note: HAADF is acquired much faster with lower dwell time and hence is noisier. (e) Profiles of the same region from the composite DF image.

the nominal value (at 0°) to varying extent. This divergence is particularly large when adjacent peaks are used in presence of tilt along the armchair axis. In the summed case, the divergence reduces significantly for tilts along both directions. This allows us to overcome the effect of small unknown tilts (< 3°) and facilitates easy interpretation.

The composite image obtained with the summed peaks is shown in Figure 6 (c) along with a virtual ADF image (b) reconstructed from the same dataset and a conventional high angle annular dark field (HAADF) STEM image (a) acquired in the same location prior to the 4D-STEM acquisition. Unlike the composite images shown in Figure 4 this composite image, made from a combination of all 6 vDF images, is much easier to interpret and does not have strange color variations within different bilayer islands.

Figure 6 (d) shows line profiles from the vADF (red) and HAADF (blue) images while (e) shows a line profile from the same region from the Ka (red) and Kb (green) composite images. The Ka and Kb profiles have similar contours while the ratio between them varies depending on orientation and stacking order of the grains. From a comparison with the vADF and HAADF profiles, we can notice that most information about orientation and stacking is lost when radially averaging the intensity at a certain scattering angle. In more detail, HAADF image is formed mainly by elastically scattered electrons inducing that image contrast varies with Z^2, only revealing the number of layers. In the vADF image, due to the presence of diffraction contrast at lower scattering angles KADF=Ka+Kb, differences between bilayer stacked 2H (AA') and 3R (AC/AB) can be discerned, however, differences between AB and AC along with information on grain orientation is lacking. This information is retained in the composite image formed using the 4D dataset which signifies the benefit of using the 4D-STEM technique over conventional (S)TEM imaging.

The general trend in intensity ratios agrees well with the CBED simulations (Fig. 7a) and enables us to uniquely assign the stacking order (in bilayer) and orientation (in monolayer) as labelled in the profile plot of fig 6. While AC stacking has the largest asymmetry between red and green channels, the asymmetry is significantly smaller and inverted for AB ($I_{Kb} > I_{Ka}$). On the other hand, AA' stacking has much higher intensity equal for both red and green channels. The 60° rotated domains in the monolayer are differentiated by the inversion of asymmetry between intensities.

Although such a composite image resulting from a combination of 6 vDF images allows for easy interpretation based on color, it is laborious to manually segment the data and get estimates of their relative abundance, specially from large areas. Therefore, in order to further automatize the data analysis so that statistically relevant information can be retrieved, a clustering procedure based on an unsupervised learning algorithm is developed. Unsupervised learning is a type of machine learning algorithm which draws inferences

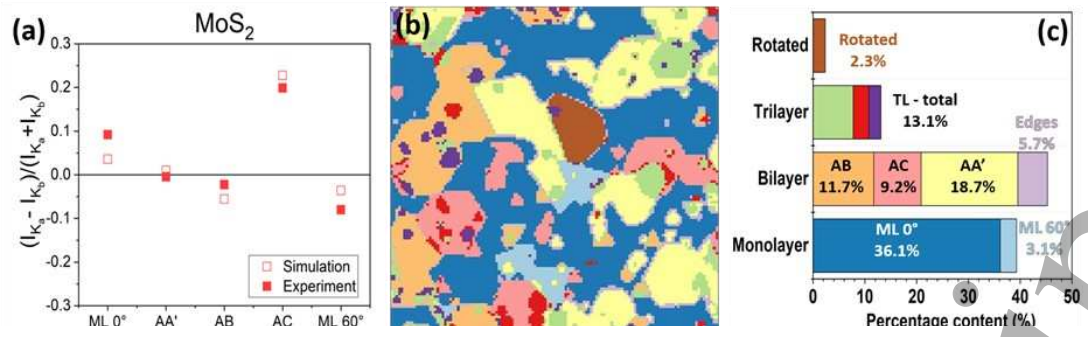

Figure 7: (a) Comparison of polarity between CBED simulations and experimental 4D-STEM data for MoS_2. (b) Segmented output from VBGM modelling. (c) Bar chart showing the abundance of various components found in the segmented image.

from an unlabelled input dataset, often used to find hidden patterns and groups in exploratory data.

Table 2: *List of mathematical operations used to form the input for the clustering model*

Category	Mathematical operation
Sum of vDF images	$Ka_{sum} = Ka_1 + Ka_2 + Ka_3$ $Kb_{sum} = Kb_1 + Kb_2 + Kb_3$
Difference	$Ka_{sum} - Kb_{sum}$ $Kb_{sum} - Ka_{sum}$
Quotient	Ka_{sum} / Kb_{sum} Kb_{sum} / Ka_{sum}
Polarity	$(Ka_1 - Kb_1)/(Ka_1 + Kb_1)$ $(Ka_2 - Kb_2)/(Ka_2 + Kb_2)$ $(Ka_3 - Kb_3)/(Ka_3 + Kb_3)$

The input provided to the VBGM model is a set of images extracted from the 4D dataset. These include two summed vDF images from the Ka and Kb diffraction spots, several mathematical operations between the two images (Table 2) and complementary vBF and vADF images extracted from the same dataset. These images are binned to 128 x 128 to reduce size for faster processing and normalized before inputting them into the model. The main parameter required by the model is the upper limit of the number of components (n) expected in the dataset which is set to 10. The algorithm then segments the data into the number of components based on correlation of features (pixel intensity in each image). The output is an array of labels provided for each pixel ranging from 0 to 9 ($n - 1$). The resulting labels are represented with different colors in the segmented image shown in Figure 7(b). The labels are then manually assigned classes and represented in the bar chart shown in Figure 7(c) where the color of the bars correspond to the segmented image. The upper limit on number of components is chosen as 10 because it is sufficiently higher than the minimum number of components required to fit the main classes of interest which include 3 for orientation in monolayer (0°, 60°and rotated to intermediate angle) and 3 for stacking in bilayer (AA', AB and AC). The remaining additional components are provided to differentiate the small regions with third layer islands. When a larger number of components are used, it results in splitting of the clusters into new components as the VBGM model tries to fit the data into as many components as are made available. These additional components are found predominantly at the interface between either ML and BL region or two differently stacked bilayer regions (similar to "edges" component shown in Fig. 7(b,c)) and are not really separate classes but instead arise as a consequence of image binning resulting in averaged intensities of pixels at the interface between two components. These interface pixels are wrongly identified as additional components when number of components provided to the model is higher than 10. This technique and the statistics obtained can be useful to evaluate growth processes which aim at the control of layer thickness, orientation and stacking of domains.

4. Conclusion

DF-TEM is shown to be a powerful technique to map the grain structure and stacking order by utilizing the asymmetry in diffraction spot intensity caused by the lack of in-plane inversion symmetry in ML and BL (AB/AC) MX_2. 4D-STEM using a direct electron detector not only helps validate the understanding from DF-TEM imaging, but also exemplifies the influence of small experimental tilts on interpretation when using only 1 or 2 conventional DF-TEM images. A simple yet effective way to overcome this issue is proposed wherein the contribution from the 3 K_a spots is summed and overlaid with the summed contribution from 3 K_b spots. A procedure is established that allows automatic segmentation of the data into n components and manually classified to obtain useful statistics about orientation and stacking. The combination of all the methods mentioned above provides crucial insights to the growers who aim to understand and tune their growth processes.

Acknowledgements

J.V. acknowledges funding from FLAG-ERA JTC2017 project "Graph-Eye". N.G. acknowledges funding from GOA project “Solarpaint” of the University of Antwerp. This project has received funding from the European Union's Horizon 2020 research and innovation programme under grant agreement No 823717 – ESTEEM3. 4D STEM data was acquired on a hybrid pixel detector funded with a Hercules fund 'Direct electron detector for soft matter TEM' from the Flemish Government. M. N. acknowledges funding from a Marie Curie Fellowship agreement No 838001. We thank Dr. Jiongjiong Mo and Dr. Benjamin Groven for developing the CVD-MoS_2 growth on sapphire and providing the material used in this article.

References

[1] Chiu K-C C, Zhang X-Q Q, Liu X, Menon V M, Chen Y-F F, Wu J-M M, Lee Y-H H, Zhang X-Q Q, Chen Y-F F, Liu X, Lee Y-H H, Chiu K-C C and Menon V M 2015 Synthesis and Application of Monolayer Semiconductors (June 2015) *IEEE J. Quantum Electron.* **51** 1–10

[2] Böker T, Severin R, Müller A, Janowitz C, Manzke R, Voß D, Krüger P, Mazur A and Pollmann J 2001 Band structure of MoS_2, $MoSe_2$ and α-$MoTe_2$ Angle-resolved photoelectron spectroscopy and ab initio calculations *Phys. Rev. B - Condens. Matter Mater. Phys.* **64** 235305

[3] Mak K F, Lee C, Hone J, Shan J and Heinz T F 2010 Atomically thin MoS_2: A new direct-gap semiconductor *Phys. Rev. Lett.* **105** 136805

[4] Ataca C, Şahin H and Ciraci S 2012 Stable, single-layer MX_2 transition-metal oxides and dichalcogenides in a honeycomb-like structure *J. Phys. Chem. C* **116** 8983–99

[5] He J, Hummer K and Franchini C 2014 Stacking effects on the electronic and optical properties of bilayer transition metal dichalcogenides MoS_2, $MoSe_2$, WS_2, and WSe_2 *Phys. Rev. B - Condens. Matter Mater. Phys.*

[6] Cheng Y, Huang C, Hong H, Zhao Z and Liu K 2019 Emerging properties of two-dimensional twisted bilayer materials *Chinese Phys. B* **28**

[7] Xia M, Li B, Yin K, Capellini G, Niu G, Gong Y, Zhou W, Ajayan P M and Xie Y H 2015 Spectroscopic Signatures of AA’ and AB Stacking of Chemical Vapor Deposited Bilayer MoS_2 *ACS Nano* **9** 12246–54

[8] Shinde S M, Dhakal K P, Chen X, Yun W S, Lee J, Kim H and Ahn J-H 2018 Stacking-controllable interlayer coupling and symmetric configuration of multilayered MoS_2 *NPG Asia Mater.* **10** e468

[9] Hovden R, Liu P, Schnitzer N, Tsen A W, Liu Y, Lu W, Sun Y and Kourkoutis L F 2018 Thickness and Stacking Sequence Determination of Exfoliated Dichalcogenides (1T-TaS_2 , 2H-MoS_2) Using Scanning Transmission Electron Microscopy *Microsc. Microanal.* **24** 387–95

[10] Sung S H, Schnitzer N, Brown L, Park J and Hovden R 2019 Stacking, strain, and twist in 2D materials quantified by 3D electron diffraction *Phys. Rev. Mater.* **3**

[11] Ryll H, Simson M, Hartmann R, Holl P, Huth M, Ihle S, Kondo Y, Kotula P, Liebel A, Müller-Caspary K, Rosenauer A, Sagawa R, Schmidt J, Soltau H and Strüder L 2016 A pnCCD-based, fast direct single electron imaging camera for TEM and STEM *J. Instrum.* **11**

[12] Wang D, Yu H, Tao L, Xiao W, Fan P, Zhang T, Liao M, Guo W, Shi D, Du S, Zhang G and Gao H 2018 Bandgap broadening at grain boundaries in single-layer MoS_2 *Nano Res.* **11** 6102–9

[13] Fatermans J, Den Dekker A J, Müller-Caspary K, Lobato I, O’Leary C M, Nellist P D and Van Aert S 2018 Single Atom Detection from Low Contrast-to-Noise Ratio Electron Microscopy Images *Phys. Rev. Lett.* **121**

[14] Xu W and LeBeau J M 2018 A deep convolutional neural network to analyze position averaged convergent beam electron diffraction patterns *Ultramicroscopy* **188** 59–69

[15] Hachtel J A, Idrobo J C and Chi M 2018 Sub-Ångstrom electric field measurements on a universal detector in a scanning transmission electron microscope *Adv. Struct. Chem. Imaging* **4**

[16] Mahr C, Müller-Caspary K, Ritz R, Simson M, Grieb T, Schowalter M, Krause F F, Lackmann A, Soltau H, Wittstock A and Rosenauer A 2019 Influence of distortions of recorded diffraction patterns on strain analysis by nano-beam electron diffraction *Ultramicroscopy* **196** 74–82

[17] Chen Z, Weyland M, Ercius P, Ciston J, Zheng C, Fuhrer M S, D’Alfonso A J, Allen L J and Findlay S D 2016 Practical aspects of diffractive imaging using an atomic-scale coherent electron probe *Ultramicroscopy* **169** 107–21

[18] Zaluzec N J 2002 Quantitative Measurements of Magnetic Vortices using Position Resolved Diffraction in Lorentz Stem *Microsc. Microanal.* **8** 376–7

[19] Clément L, Pantel R, Kwakman L F T and Rouvière J L 2004 Strain measurements by convergent-beam electron diffraction: The importance of stress relaxation in lamella preparations *Appl. Phys. Lett.* **85** 651–3

[20] Hirata A, Guan P, Fujita T, Hirotsu Y, Inoue A, Yavari A R, Sakurai T and Chen M 2011 Direct observation of local atomic order in a metallic glass *Nat. Mater.* **10** 28–33

[21] Ozdol V B, Gammer C, Jin X G, Ercius P, Ophus C, Ciston J and Minor A M 2015 Strain mapping at nanometer resolution using advanced nano-beam electron diffraction *Appl. Phys. Lett.* **106**

[22] E H, MacArthur K E, Pennycook T J, Okunishi E, D’Alfonso A J, Lugg N R, Allen L J and Nellist P D 2013 Probe integrated scattering cross sections in the analysis of atomic resolution HAADF STEM images *Ultramicroscopy* **133** 109–19

[23] Tao J, Niebieskikwiat D, Varela M, Luo W, Schofield M A, Zhu Y, Salamon M B, Zuo J M, Pantelides S T and

Pennycook S J 2009 Direct imaging of nanoscale phase separation in $La_{0.55}Ca_{0.45}MnO_3$: Relationship to colossal magnetoresistance *Phys. Rev. Lett.* **103**

[24] Liu A C Y, Neish M J, Stokol G, Buckley G A, Smillie L A, De Jonge M D, Ott R T, Kramer M J and Bourgeois L 2013 Systematic mapping of icosahedral short-range order in a melt-spun $Zr_{36}Cu_{64}$ metallic glass *Phys. Rev. Lett.* **110**

[25] Gallagher-Jones M, Ophus C, Bustillo K C, Boyer D R, Panova O, Glynn C, Zee C-T, Ciston J, Mancia K C, Minor A M and Rodriguez J A 2019 Nanoscale mosaicity revealed in peptide microcrystals by scanning electron nanodiffraction *Commun. Biol.* **2**

[26] Chiappe D, Ludwig J, Leonhardt A, El Kazzi S, Nalin Mehta A, Nuytten T, Celano U, Sutar S, Pourtois G, Caymax M, Paredis K, Vandervorst W, Lin D, De Gendt S, Barla K, Huyghebaert C, Asselberghs I and Radu I 2018 Layer-controlled epitaxy of 2D semiconductors: Bridging nanoscale phenomena to wafer-scale uniformity *Nanotechnology* **29**

[27] Nalin Mehta A, Mo J, Pourtois G, Dabral A, Groven B, Bender H, Favia P, Caymax M and Vandervorst W 2020 Grain-Boundary-Induced Strain and Distortion in Epitaxial Bilayer MoS_2 Lattice *J. Phys. Chem. C* **124** 6472–8

[28] Koch C T 2002 Determination of core structure periodicity and point defect density along dislocations *Dissertation*

[29] Pedregosa F, Varoquaux G, Gramfort A, Michel V, Thirion B, Grisel O, Blondel M, Prettenhofer P, Weiss R, Dubourg V, Vanderplas J, Passos A, Cournapeau D, Brucher M, Perrot M and Duchesnay E 2011 Scikit-learn: Machine Learning in Python *J. Mach. Learn. Res.* **12** 2825–30

[30] Zhao X, Ding Z, Chen J, Dan J, Poh S M, Fu W, Pennycook S J, Zhou W and Loh K P 2018 Strain Modulation by van der Waals Coupling in Bilayer Transition Metal Dichalcogenide *ACS Nano* **12** 1940–8

[31] Mortelmans W, Nalin Mehta A, Balaji Y, El Kazzi S, Sergeant S, Houssa M, De Gendt S, Heyns M and Merckling C 2020 Fundamental limitation of van der Waals homoepitaxy by stacking fault formation in WSe_2 *2D Mater.* **7** 025027

[32] Deb P, Han Y, Xie S, Holtz M E, Park J and Muller D A 2017 Breaking Friedel's Law in Polar Two Dimensional Materials *Microsc. Microanal.* **23** 1738–9

[33] Johnstone D N, Crout P, Laulainen J, Høgås S, Martineau B, Bergh T, Smeets S, Collins S, Morzy J, Ånes H W, Prestat E, phillipcrout, Doherty T, Ostasevicius T, Mohsen, EirikOpheim, Tovey R and Jacobsen E 2020 pyxem/pyxem: pyxem 0.10.1